Steric confinement for suppressing ion migration and boosting thermoelectric performance in Cu–S system via Ag and Se co-doping

Xinyuan Wang, Cédric Bourgès, Jean-Claude Crivello, Takao Mori

Acta Materialia 299 (2025) 121424

Contents lists available at ScienceDirect

Acta Materialia

journal homepage: www.elsevier.com/locate/actamat

Full length article

Steric confinement for suppressing ion migration and boosting thermoelectric performance in Cu–S system via Ag and Se co-doping

Xinyuan Wang [a,b], Cédric Bourgès [c,d,*], Jean-Claude Crivello [e], Takao Mori [a,b,*]

[a] Research Center for Materials Nanoarchitectonics (MANA), National Institute for Materials Science (NIMS), Namiki 1-1, Tsukuba 305-0044, Japan
[b] Graduate School of Pure and Applied Sciences, University of Tsukuba, 1-1-1 Tennoudai, Tsukuba 305-8577, Japan
[c] International Center for Young Scientists (ICYS), National Institute for Materials Science, 1-1 Namiki, Tsukuba, 305-0044, Japan
[d] Univ. Limoges, CNRS, IRCER, UMR 7315, F-87000 Limoges, France
[e] CNRS-Saint-Gobain-NIMS, IRL 3629, Laboratory for Innovative Key Materials and Structures (LINK), 1-1 Namiki, 305-0044 Tsukuba, Japan

ARTICLE INFO

Keywords:
Cu-S System
Steric confinement
Thermal stability
Electrical stability
Thermoelectric

ABSTRACT

The Cu-S superionic compound exhibits excellent thermoelectric (TE) performance in the mid-temperature region. However, obtaining a thermally and electrically stable material in this system is still challenging. Herein, motivated by the perspective of steric confinement for suppressing Cu^+ migration, we designed an Ag and Ag-Se co-doping strategy on pristine $Cu_{1.93}S$ to modulate the crystal structure. On one hand, Ag dopant is discovered to act as a vacancy filler, simultaneously optimizing carrier concentration and reducing thermal conductivity. Moreover, strategic Se co-substitution stabilizes Ag insertion within the Cu-S vacancy and induces non-negligible enhancement of phonon scattering to further reduce thermal conductivity. A competitive peak zT of 1.33@873 K was obtained for the $Cu_{1.93}Ag_{0.04}S_{0.9}Se_{0.1}$ sample at a relatively moderate temperature among current state-of-the-art Cu-S system. Moreover, thanks to the steric confinement, the $Cu_{1.93}Ag_{0.04}S_{0.9}Se_{0.1}$ composition exhibited superior electrical stability under dynamic DC-current compared to Cu_xS (with $1.93<x<1.97$), indicating that Ag and Ag-Se co-doping are effective at suppressing the electromigration of Cu^+. Furthermore, an improved thermal stability of $Cu_{1.93}Ag_{0.04}S_{0.9}Se_{0.1}$ was attributed to percolated Ag which confines sulfur evaporation by strengthening the chemical bonding. In addition, a first-principles study demonstrates that the addition of Ag and Se creates new electronic interactions with their nearest neighbors and also modifies the local atomic environment by increasing interatomic distances, which contributes to limiting Cu diffusion and improving thermoelectric stability. Through the method of steric confinement via Ag insertion and Se doping in the $Cu_{1.93}Ag_xS_{1-y}Se_y$ system, we achieved a desirable combination of high TE performance and notable thermal and electrical stability.

1. Introduction

Efficiently using waste energy can play a key role in developing new environmentally friendly energy sources. With the benefit of converting thermal energy into electrical energy directly and reversibly without emitting carbon dioxide, thermoelectric (TE) devices have attracted much attention in the field of sustainable energy [1–4]. The energy conversion efficiency for TE devices can be determined by the dimensionless figure of merit zT, which is defined as $zT = \alpha^2\sigma T/(\kappa_L + \kappa_e)$, where T, α, σ, κ_L, κ_e are the absolute temperature, Seebeck coefficient, electrical conductivity, lattice thermal conductivity, and carrier thermal conductivity, respectively [3]. Currently, the highest TE performances have been obtained as example for the compounds Bi_2Te_3 [5–7], PbTe [8], GeTe [9], SnSe [10] to cite a few. However, based on the advances of low-cost, non-toxic and environmentally friendly alternatives materials, the magnesium-based [11,12] and copper-based TE materials [13–20] are attracting increasing attention. Among the copper-based system, binary copper sulfides ($Cu_{2-x}S$), which have been investigated approximately for 200 years, show a competitive thermoelectric performance in the middle-temperature region (ex. $Cu_{1.97}S$, $zT = 1.7$@1000 K) [21,22] due to the tuned phonon anharmonicity [23]. However, as a superionic conductor, it still presents challenges due to its ionic and thermal instability over long operating periods [24,25]. Thus, a comprehensive consideration of the stability and thermoelectric properties of the materials is a major prerequisite for achieving a technological breakthrough.

* Corresponding authors.
E-mail addresses: cedric.bourges@unilim.fr (C. Bourgès), MORI.Takao@nims.go.jp (T. Mori).

https://doi.org/10.1016/j.actamat.2025.121424
Received 24 April 2025; Received in revised form 28 July 2025; Accepted 8 August 2025
Available online 9 August 2025

According to the Copper-Sulfide binary phase diagram, four typical room temperature phases could be found: the Covellite (CuS), Digenite ($Cu_{1.8}S$), Djurleite ($Cu_{1.93}S$ - $Cu_{1.96}S$) and Chalcocite (Cu_2S). Among them, CuS exhibits poor TE potential between 323 K and 573 K, and structural investigation also reveals a non-reversible phase transition at temperatures above 453 K. Thus, in addition to its low TE properties, this confirms that CuS is not suitable for TE applications. The $Cu_{1.8}S$ shows a great ionic stability under the high current density (48 A/cm^2) at room temperature, which makes it attractive in the Cu-S system [24]. As reported by *Ge et al.*, the pristine $Cu_{1.8}S$ could achieve a $zT = 0.3$ at 673 K which is relatively modest for the mid-temperature applications [26]. Subsequent reports have been devoted to optimize TE property based on $Cu_{1.8}S$ in the higher temperature region (673 K to 773 K). Notably, doping or compositing strategy in this compound tends to always create the typical secondary $Cu_{1.96}S$ phase which could provide much higher TE performance [27–32]. However, in our previous works, we demonstrated an irreversible phase transition from $Cu_{1.8}S$ to $Cu_{1.96}S$ induced by a slight sulfur evaporation during high temperature treatment over long period [33]. Nevertheless, we showed the path to partially reduce the degradation, thanks to the selection of suitable synthesis methods. On the other hand, Cu_2S shows excellent TE performance ($Cu_{1.97}S$: $zT = 1.7$@1000 K) after controlling its Cu vacancy framework [21]. However, a large performance degradation happens even under low current stress (12 A/cm^2) because of its superionic character creating a critical problem when using in TE devices [24]. To address the issue of copper degradation in Cu_2S, several influential studies have focused on compositing with insulating phases. such as Cu_2S-In_2S_3 [34] or with quartz [35] to effectively block the Cu migration. This results in excellent electrical stability at high temperatures and competitive TE performance, which confirms the importance of adopting a strategy aimed at optimizing both electrical stability and TE performance.

The superionic behavior of $Cu_{2-x}S$ is characterized by the migration of copper ions within a relatively rigid sulfur sublattice when subjected to external stimuli such as electrical or thermal potential. This phenomenon arises from the low activation energy for electromigration (approximately 0.19 eV in Cu_2S), enabling Cu^+ to exhibit high diffusivity. As a result, these ions behave in a manner akin to a liquid, rapidly hopping between energetically favorable sites while the anion framework remains largely stationary [25]. To effectively suppress ion migration and improve the thermal and structural stability of $Cu_{2-x}S$--based materials, steric confinement was proposed in this study. By introducing dopants with larger ionic radii, local lattice distortion can be created, which in turn hinders the mobility of Cu^+ through spatial restrictions. This confinement effect not only elevates the activation barrier for ion hopping [36], thereby suppressing cationic migration, but also enhances phonon scattering due to the possible lattice strain [37], ultimately contributing to lower lattice thermal conductivity and improved thermoelectric performance. As mentioned before [24,33], the Cu–S binary system presents challenges related to thermal instability and excessive Cu^+ migration at elevated temperatures. To address these limitations and potentially achieve improved thermal stability compared to the $Cu_{1.8}S$ and reduced Cu^+ migration compared to the Cu_2S, djurleite ($Cu_{1.93}S$–$Cu_{1.96}S$) was selected as the initial target phase. In particular, $Cu_{1.93}S$—the composition with the lowest Cu/S ratio in the homogeneity range, was chosen to maximize doping capability. Guided by the concept of steric confinement, Ag^+ with larger ionic radii were introduced as interstitial fillers, while Se atoms served as anionic substitutes. A systematic experimental and theoretical investigation was conducted to evaluate the effects of Ag doping and Ag–Se codoping on the structural, microstructural, thermoelectric, and stability properties of the Cu–S system.

2. Experimental sections

2.1. Preparation

The stoichiometric proportions of copper (Cu, 99.95 %, powder, Kojundo Chemical Laboratory Co., Ltd.) and sulfur (S, Sigma Aldrich, 99.99 %, flakes) and silver (Ag, Sigma Aldrich, 99.95 %, powder) and selenium (Se, Sigma Aldrich, 99.95 %, powder). The powder was set in a 45 ml tungsten carbide (WC) jar with 14 × 10 mm WC ball. Milling was performed at the planetary ball milling machine (Pulverisette P7-Premium line) at 600 rpm for 2 h under Ar atmosphere. The mass ratio of the total ball and total powder was 20: 1. After milling the powder was kept in an Ar-filled glovebox. The resulting powders were loaded into a ϕ 10 mm graphite die prepared in advance with carbon paper coated by BN layer. The powders were then densified by spark plasma sintering (SPS) at 973 K (heating/cooling rate 100 K/min) under a uniaxial pressure of 50 MPa keeping for 5min. All the sample's densities were higher than 95 % of the theoretical.

2.2. Structural and chemical characterization

The regular crystal structure was determined by X-ray diffraction (XRD) with the prescriptive θ–2θ mode with the angular range of 5°–120° (Smart Lab 3 Rigaku Corporation). The high-temperature crystal structure was determined by high temperature X-ray diffraction (HT-XRD) technique with the prescriptive θ–2θ mode with the angular range of 5° – 120° (Rigaku SmartLab 9 kW) from 300 K to 773 K during heating and cooling. The thermal stability of digenite samples were investigated by thermogravimetric/dynamic scanning calorimetry (TG/DSC, STA 449 F1 Jupiter, Netzsch), the heating rate was 10 K/min and the measurements were performed under Ar atmosphere. Observations of the component analysis were proceeded by energy dispersive spectroscopy (EDS) on mirror polished surface with a Hitachi TM3000 Tabletop SEM.

2.3. Thermoelectric property measurement

The temperature dependence of the electrical conductivity σ and Seebeck coefficient α were measured by the ULVAC-ZEM3 system under a partial helium atmosphere from 300 K up to 873 K. The thermal conductivity was calculated according to $\kappa = \lambda C_p \rho$, where κ represents the total thermal conductivity, λ is the thermal diffusivity, C_p is the heat capacity, and ρ is the measured density. Thermal diffusivities (λ) of each sample were measured by LFA-457 Laser Flash with an estimated error of ca. 5 %. The temperature-dependent C_p values were calculated by Dulong et Petit law. Density (ρ) values were measured by the Archimedes' method. The uncertainty in the results was estimated to be 6 % and 8 %, respectively for the α and σ, giving an overall 11 % on the *PF*. The uncertainty on the thermal transport properties is 10 %, and that for the overall zT was 17.5 % [35]. The carrier concentration and mobility were obtained from Hall Effect measurements in AC transport by using a PPMS (Quantum design) from -5 to +5 T.

2.4. Current stress test

The current stress test was carried out using a home-built testing system composed of a direct current supply (AS ONE, DCP3005, Japan), alumina ceramic substrate, nickel electrode, several clamps and wires. A close circuit of the sample was assembled before the test. During the test, the current density were controlled by the direct current supply and the measurements were under vacuum condition. The resistivity of each sample was measured via the four-probe mode of a commercial measuring system (ZEM-3, Ulvac-Riko, Japan) under the low current density (<1 mA) to exclude the temperature effect due to the Peltier effect.

2.5. Computational methods

To model different compositions and estimate their phase stability, several disordered $Cu_xAg_{x'}Va_{2-x-x'}S_{1-y}Se_y$ compounds were considered in the cubic *Fm*-3*m* structure using 2 × 2 × 2 and 2 × 2 × 6 supercells containing 96 and 288 atoms, respectively, to express several $x \sim 2$ and $y = 0.01$ and 0.1 for $x = 1.94$ (Fig. S1). Additionally, the hexagonal $P6_3/mmc$ chalcocite structure was modeled using a supercell containing up to 128 atoms without the vacancies *VA* (Fig. S2). For the cubic phase, to simulate $x = 1.96$ and $x = 1.93$, the distribution of 2-*x*-*x*' Cu-vacancies and *x*' Ag substitutions was generated using several *ad hoc* configurations, considering the extreme distance possibilities between end-member compounds, both with and without symmetry breaking. For the hexagonal $Cu_xAg_{x'}Va_{2-x-x'}S$ phase, a similar strategy was applied to distribute vacancies and Ag atoms. However, to deal with the partial occupancies of Cu in its sites, the construct of the initial Cu_2S initial compound was made by the Special Quasirandom Structures (SQS) method [38] using the Alloy Theoretic Automated Toolkit (ATAT) [39, 40]. This approach was considered to generate possible vacancy distributions across both Cu1 (12*k*) and Cu2 (2*b*) sites, with rounded occupancies of 5/8 and 3/4, respectively. Specifically, 32 atoms were removed from a 128-atom supercell to obtain the initial Cu_2S configuration with 96 atoms, in which S atoms are fixed at the 2*c* positions, resulting in a 64:32 Cu:S atomic ratio within the modeled supercell. The SQS method approximates the random distribution of elements in disordered way by considering local atomic clusters, in our case by including eight first-neighbor pairs, three triangles, and a tetrahedron. The $y = 0.01$ and 0.1 Se substitutions was only considered starting from the cubic description by brute force approach: Fig. S3 illustrates examples of 2 × 2 × 6 supercells generated using the most stable $x = 1.94$ and $x' = 0.03$ compound to model $Cu_{1.94}Ag_{0.03}Va_{2-x-x'}S_{0.99}Se_{0.01}$ and $Cu_{1.94}Ag_{0.03}Va_{2-x-x'}S_{0.90}Se_{0.10}$ compounds using all the most extreme cases of atoms distribution (from about 20 different samples).

First-principles calculations were performed using the Vienna Ab Initio Simulation Package (VASP) [41], implementing in the Density Functional Theory (DFT) framework. The generalized gradient approximation (GGA) with the Perdew-Burke-Ernzerhof (PBE) [42] functional was used for total energy calculations, while the modified Becke-Johnson (mBJ) exchange-correlation functional was employed for electronic band structure calculations [43]. A plane-wave basis set with an energy cutoff of 600 eV was applied. A high-density k-point mesh was used ($k_I \cong 0.05 \times \frac{2\pi}{a_i}$) to ensure accurate Brillouin zone sampling. The convergence criterion for the self-consistency loop was set to 10^{-4} eV, ensuring precise wave function optimization.

During relaxation, atomic positions, cell shape (while preserving original symmetry), and volume were optimized to account for small distortions in disordered phases. While the volumes of cubic-derived structures are simply relaxed with isotropic dilation, the hexagonal cell shape requires additional adjustments for the *c*/*a* ratio, as triclinic SQS cells lack orthogonal basis vectors. To maintain the original shape, a dilation matrix aligned with the basis vectors was applied throughout the relaxation process.

Phonon calculations were performed using the harmonic approximation within the framework of the frozen phonon method, incorporating relevant atomic displacements generated by the phonopy code [42]. In the case of the cubic structures, this process led to 34 displacements starting from the considered structure which was relaxed within a force threshold of 5.10-5 eV/Å.

3. Result and discussion

3.1. Synthesis and structural analysis

The crystal structure of copper-rich low djurleite and chalcocite at room temperature can be visualized as simple close-packed rigid sulfur framework randomly jammed by copper atoms. The clustering of vacancies and Cu atoms with different occupancies will create several substructural descriptions [44–46], such as tetragonal for $Cu_{1.96}S$ (PDF#00-029-0578) with space group $P4_32_12$, monoclinic for $Cu_{31}S_{16}$ (PDF#00-072-0634) with space group $P2_1/n$ or monoclinic for Cu_2S (PDF#01-083-1462) with space group $P2_1/c$. To synthesis the Ag and Ag-Se co-doped samples, we used a reactive synthesis approach by coupling a mechanical alloying step of pure elements (Cu, Ag, S, Se) with a Spark Plasma Sintering (SPS) densification. Due to the reactive aspect of the synthesis, the structural stability of the resulting pellets could be a concern. Consequently, we characterized the as synthesized samples and after aging dependence (60 days) of room temperature XRD (Fig. 1a–c) for the typical three representatives' samples ($Cu_{1.93}S$, $Cu_{1.93}Ag_{0.04}S$ and $Cu_{1.93}Ag_{0.04}S_{0.9}Se_{0.1}$) after SPS. It should be noted that all the samples were crushed into fine powders uniformly to eliminate the influence of preferred orientation and/or surface effect. The pristine $Cu_{1.93}S$ sample (Fig. 1a) after SPS sintering was found to be metastable: the pristine XRD pattern revealed initially a major tetragonal phase (PDF#00-029-0578) with a minor amount of monoclinic phase (PDF#00-072-0634) but, after being aged 60 days at room temperature under vacuum atmosphere, the ratio between tetragonal and monoclinic phase was totally reversed into a major monoclinic phase with a minor amount of tetragonal phase. This finding is consistent with similar phase transformation reported in literature [45]. Interestingly, we evidenced that Ag doping prevents the formation of the metastable tetragonal structure after the reactive process (Fig. 1b and Fig. S4a). As example in the case of $Cu_{1.93}Ag_{0.04}S$ sample, the as-synthesized sample crystal structure could be mostly described by a mixture of the two common monoclinic structures of $Cu_{31}S_{16}$ (PDF#00-029-0578) and Cu_2S (PDF#01-083-1462). After the aging time, the relative intensity of the mains peaks slightly changed toward the solely $Cu_{31}S_{16}$ structure formation, which indicates that Ag doping stabilizes monoclinic lattice but does not fully cancel the post-SPS metastability [46]. In the case of Ag-Se co-doping, the samples retain the mixed stable monoclinic structure after aging (Fig. 1c and Fig. S1b), confirming that the substitution of S (1.04 Å) by Se (1.16 Å), which has a larger atomic radius, increase the local steric stress of the lattice thereby stabilizing the monoclinic structure which led to fully eliminate the as-synthesized metastability. It is worth noting that a simple aging investigation on the crystal structure under the vacuum and room temperature showed that introducing Ag and Se into $Cu_{1.93}S$ would be helpful for transferring the metastable tetragonal phase to the stable monoclinic phase and improving the apparent structural stability of the binary compound.

To sustain the proper insertion of the Ag within the structure as well as the Ag-Se codoping and investigate their respective effects on the crystal structure, the HT-XRD and systematic SEM-EDX were performed in the as-synthesized and annealed samples. The HT-XRD analysis has been performed in three representative bulk samples as displayed in the Fig. 1d–f. First, we analyzed the pattern at 773 K by Le Bail refinement wherein the samples adopt the well-known cubic structure. All samples displayed single-phase patterns with an apparent main diffraction peak shifted toward the low angle (Fig. S5-inset) attesting that the lattice parameter enlarged. Le Bail refinement confirmed a clear increase in lattice parameters from 5.675(1) Å for the pristine $Cu_{1.93}S$, to 5.709(1) Å for the Ag-doped sample and further increased up to 5.734(1) Å with the Ag-Se codoped sample. It is agreed with the larger atomic radius of Ag and Se would substitute the Cu vacancy and S site and consequently expand the lattice. The proper insertion of Ag and the codoping of Ag-Se is corroborated by the Energy Dispersive X-ray (EDX) analysis after annealing which confirms a homogeneous distribution of the Ag and the Ag-Se elements within the matrix in the doped samples (Fig. S6). It can be observed that, only in the case of the as-synthesized $Cu_{1.93}Ag_{0.04}S$, the SEM-EDX analysis revealed a mixture of $Cu_{2-x}S$ and $Ag_{2-x}S$ phases (Fig. S6c) nearly impossible to separate in the XRD (Fig. S4a), this is most likely attributed to kinetic limitations and incomplete elemental diffusion during the rapid SPS process. However, during the high

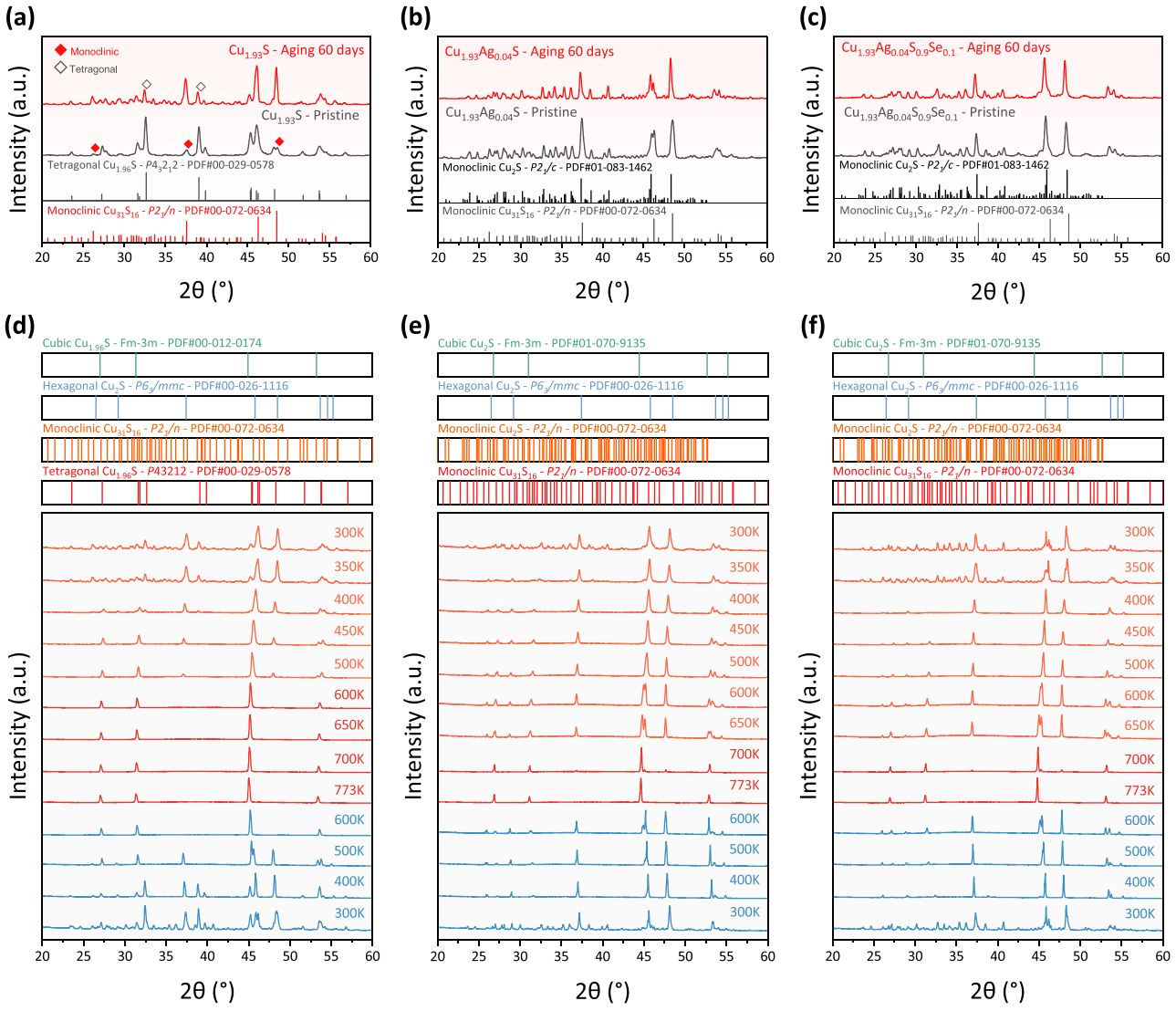

Fig. 1. Aging dependence (the pulverized powder was stored under vacuum for 60 days) of room temperature XRD for bulk samples (a) $Cu_{1.93}S$, (b) $Cu_{1.93}Ag_{0.04}S$ and (c) $Cu_{1.93}Ag_{0.04}S_{0.9}Se_{0.1}$ and its respective HT-XRD (Heating in red and cooling in blue) patterns (d, e, f).

temperature stage (> 450 K), the typical satellite peak of Ag_2S did not appear (Fig. S5), which indicates that the Ag re-dissolved in the Cu lattice and confirmed that the samples is properly doped. Furthermore, an annealing experiment was carried out at 773 K for 30 minutes under N_2 atmosphere to simulate the actual thermal environment during measurement. EDX analysis after annealing showed a more uniform distribution of Cu, Ag, S, and Se elements in both $Cu_{1.93}Ag_{0.04}S$ and $Cu_{1.93}Ag_{0.04}S_{0.90}Se_{0.10}$ compared to the as-synthesized samples. This further supports that annealing promotes elemental homogenization and facilitates the effective incorporation of Ag into the Cu-based lattice. Notably, after annealing, the Se-doped sample ($Cu_{1.93}Ag_{0.04}S_{0.90}Se_{0.10}$) exhibited a more uniform and stable distribution of Ag compared to the undoped counterpart ($Cu_{1.93}Ag_{0.04}S$), further highlighting the beneficial role of lattice expansion in enhancing Ag solubility.

Besides the doping confirmation, the careful analysis of the HT-XRD of all the three samples revealed that all samples undergo two well-known phase transitions: the monoclinic to hexagonal structure and then the hexagonal to cubic structure. However, the transition temperature varies significantly between the pristine $Cu_{1.93}S$ and Ag/Ag-Se codoping. As a reference, the pristine $Cu_{1.93}S$ started from a mixed tetragonal-monoclinic phase as described by the former section, and turn to the hexagonal form ($P6_3/mmc$; $a \approx 3.961$ Å, $c \approx 6.722$ Å, PDF#00-026-1116) at around 400 K and in the cubic ($Fm\bar{3}m$; $a \approx 5.707$ Å, PDF#00-012-0174) at around 600 K which corresponds to the high temperature form of the $Cu_{2-x}S$ system ($x < 0.01$-0.2) (Fig. 1d). The heating and cooling cycle appeared non-reversible as the cooling to room temperature favorize the re-formation of the metastable tetragonal form. For the $Cu_{1.93}Ag_{0.04}S$ and $Cu_{1.93}Ag_{0.04}S_{0.9}Se_{0.1}$ samples, the monoclinic to hexagonal structural transition occurred gradually at slightly reduced temperature from 300 K to 400 K and the final cubic phase transition can be observed at 700 K in excellent agreement with the DSC (Fig. S7). Moreover, consistently with the aging test observation, the room temperature structure appeared more stable than the undoped sample and a reversibility of the phase transition is observed during cooling toward the as-synthesized/aged monoclinic structure. It evidences once more that Ag insertion alters the fundamental structural stability of the $Cu_{2-x}S$ structures.

To further understand the effect of Ag and Se, we conducted a theoretical investigation using first principles calculations. For this, it was essential to select the modeled structure $Cu_xAg_{x'}Va_{2-x-x'}S_{1-y}Se_y$ with the defects we intend to simulate, i.e. $x_{Cu} = \{1.94, 1.97, 2\}$ and $x'_{Ag} = 0.03$ for $x_{Cu} = 1.94$ and $y_{Se} = \{0.01, 0.10\}$ with $x'_{Ag} = 0.03$, as shown in Fig. 2. Due to the impossibility to build an accurate and robust model of the room temperature structural forms (monoclinic and tetragonal),

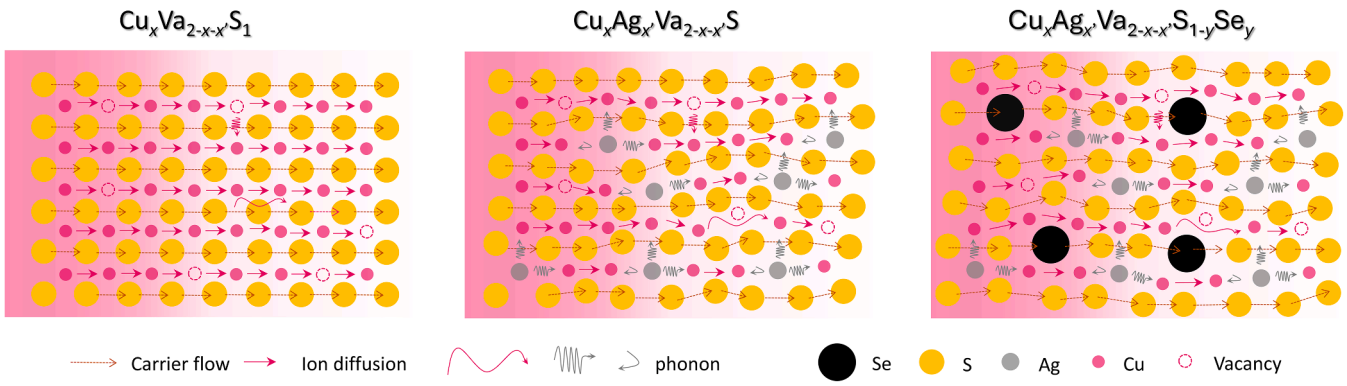

Fig. 2. Modeled structure from $Cu_xVa_{2-x-x'}S$ to $Cu_xAg_{x'}Va_{2-x-x'}S$ and $Cu_xAg_{x'}Va_{2-x-x'}S_{1-y}Se_y$, the potential scattering and ionic diffusion have been indicated.

these latter have not been considered in the current investigation. Therefore, for each type of defect or desired substitution, multiple supercell structures were constructed in hexagonal and cubic descriptions and tested using the DFT calculations to estimate their relative formation energy, defined as the energy difference between its total energy and the sum of the energies of its constituent pure elements, normalized by the total number atoms in the considered cell. Compared to a previous study by Mikula made on Cubic phase [47], we tested symmetry-breaking approaches for different compositions. We observed that symmetric representations tend to yield more stable configurations. Additionally at a given composition, it is noteworthy that the hexagonal phase is lower in energy compared to the cubic form, as expected from experimental phase equilibrium studies. The cubic phase, which is stabilized at higher temperatures, exhibits an energy difference ranging from 3.9 to 3.2 kJ/mol as the concentration of vacancies increases (Fig. S8). For each Cu composition $x_{Cu} = \{2, 1.94, 1.97\}$, the most stable cubic configuration was analyzed with respect to the Cu environment. The average distance of the four nearest Cu-S neighbors in the relaxed cell was found to be 2.416, 2.409, and 2.412 Å, respectively. While these values are very close, a noticeable change occurs in the Ag-doped compounds, where the Cu-S distance increases slightly to 2.418 Å. Furthermore, the Ag-S bond length is significantly larger due to the increased atomic size of Ag, with an average Ag-S distance of 2.591 Å for $Cu_{1.94}Ag_{0.03}S$. Starting from the most stable Ag-doped compound model (Fig. S1), numerous simulations were performed to identify the most favorable sulfur atom to be substituted by selenium within a 285-atom supercell, in order to reproduce a composition of $y_{Se} = 0.01$. The most stable co-doping configuration corresponds to Se occupying a first-neighbor position relative to Ag (Fig. S9). While the Cu–S and Ag–S bond lengths remain similar to those in the Ag-only doped structure, the substitution of S by Se increases the pair distances to 2.610 Å and 2.659 Å for Cu–Se and Ag–Se, respectively. Based on this configuration, a new supercell for $y_{Se} = 0.1$ was constructed to match the experimental composition. The final DFT relaxation of this $y = 0.1$ Se co-doped compound leads to a general volume increase of approximately 3.5 % compared to the structure without Se. In conclusion, the use of dopants not only has an electronic effect, which will be further illustrated in Section 3.2, but also has a steric confinement effect by increasing interatomic distances, as the diffusion of Cu^+ is strongly influenced by the geometry and continuity of the migration pathways within the lattice. Experimentlly, the incorporation of larger atoms of Ag^+ and Se^{2-} leads to lattice expansion, as confirmed by the increased lattice parameters observed in our HT-XRD results (Fig. S5). This expansion alters the Cu–Cu distances which could limit ion migration by elongating the hopping distance combined with the steric confinement introduced by larger dopants to increase the migration energy barrier for Cu^+.

3.2. Band structure

For each unique composition, the most stable models obtained using GGA were retained to analyze the corresponding electronic structure with the mBJ meta-GGA functional. This approach is known to provide a more accurate estimation of electronic band gaps, which is the case in our system studied by comparing the GGA and mBJ band structures (comparison not shown). As shown in Fig. 3, the band structures are generally very flat for all these compounds, reflecting the predominantly localized nature of the copper 3*d* states. The sulfur *s-p* states exhibit low-energy features, starting around 7 eV below the Fermi level, with a band gap of approximately 2 eV in the cubic phases, whereas in the hexagonal form, the conduction bands form almost continuously occupied states. The chemical bonding is predominantly ionic-covalent, with a charge transfer of approximately 0.8 electrons from the filled *d* bands of Cu/Ag to S/Se, as estimated by Bader analysis (Table 1). This effect is even more pronounced in the cubic phase compared to the hexagonal form. An increase of the Cu vacancies (decreased of the Cu concentration) leads to a slight reduction in the effective charge on sulfur.

Especially in the high-temperature cubic phase, the addition of Ag leads to the formation of low-energy 4*d* bands around -4 eV, below the 3*d* states of copper, which may play a role in limiting metal diffusion by raising an energy barrier. At the very low compositions studied, the presence of vacancies or elemental substitutions (Ag, Se) has finally minor impact on the overall electronic structure but does influence properties near the Fermi level. Indeed, starting from the ideal Cu_2S compound, the presence of vacancies, *i.e.*, a decrease in *x*, induces modifications in the band gap with a slight enlargement, most visible in the hexagonal form. The gap is estimated to be around 0.8 eV for $Cu_{1.94}S$ in its hexagonal form even with the mBJ model which is still underestimated in comparison with the experimental one. In the cubic form, the Density of State (DOS) seems to have a similar behavior with a value "remaining close to zero" as claimed in the DOS analysis of Mikula, but there is a crossing dispersed band at the gamma point, corresponding to the interaction of *s*-states of Cu with S.

Electronic band structure calculation has been performed on the $Cu_{1.94}Ag_{0.03}VA_{0.03}S_{0.99}Se_{0.01}$ and $Cu_{1.94}Ag_{0.03}VA_{0.03}S_{0.10}Se_{0.10}$ composition in the cubic form, corresponding to the best TE performance obtained, to estimate the influence of the Ag-Se codoping (Fig. 4). The metallic character becomes even more pronounced with Se substitution, which not only reduces the band gap at the Fermi level but also induces band degeneracy, creating new states along the Γ–M direction resulting in enhanced metallicity (Fig. 4). Additionally, Se influences the structure through interactions between its *s-p* states and those of its nearest neighbors (Ag and Cu) which is expected to contribute to limiting the Cu diffusion. This effect can be attributed to the enhanced hybridization between the Se 4*p* orbitals and the *s/d* orbitals of neighboring Cu and Ag atoms, which strengthens the local bonding environment and increases the energy barrier for Cu migration, thereby suppressing its diffusion.

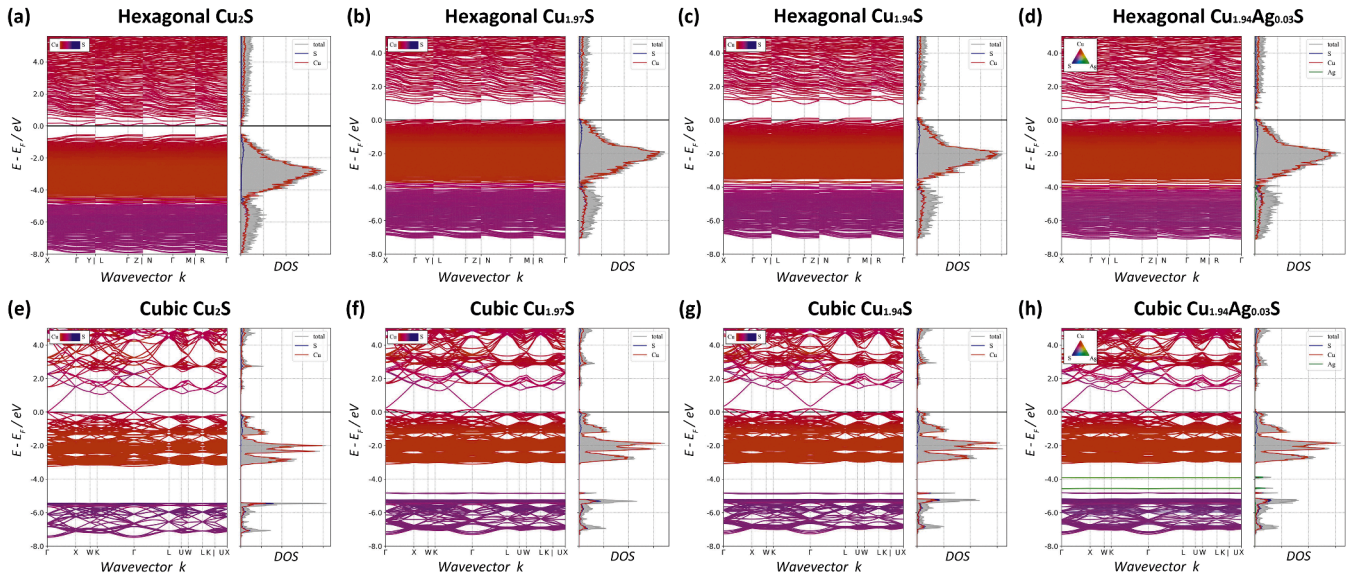

Fig. 3. Electronic band structure at key symmetry points of $Cu_xAg_{x'}Va_{2-x-x'}S$ for $x = \{1.94, 1.97, 2\}$ and $x' = 0.03$, along with the corresponding projected density of states (DOS) in hexagonal and cubic symmetries. Results obtained using mBJ functional. The Fermi level is set as the energy reference.

Table 1
DFT results for all most stable $Cu_xAg_{x'}Va_{2-x-x'}S_{1-y}Se_y$ compounds investigated in this work, according to Pristine (cubic) or chalcocite (hexagonal) form: enthalpy of formation and electronic charge transfer.

$Cu_xAg_{x'}Va_{2-x-x'}S_{1-y}Se_y$ compounds			Bader (electron charge)			
Composition	Symmetry	ΔH_f (kj/mol)	Cu	Ag	S	Se
Cu_2S	cubic	-5.248	0.447		-0.895	
$Cu_{1.97}S$	cubic	-6.214	0.443		-0.872	
$Cu_{1.94}S$	cubic	-7.122	0.448		-0.868	
$Cu_{1.94}Ag_{0.03}S$	cubic	-5.790	0.443	0.266	-0.866	
$Cu_{1.94}Ag_{0.03}S_{0.99}Se_{0.01}$	cubic	-5.975	0.444	0.258	-0.870	-0.683
$Cu_{1.94}Ag_{0.03}S_{0.10}Se_{0.10}$	cubic	-6.369	0.432	0.265	-0.862	-0.708
Cu_2S	hexagonal	-9.125	0.373		-0.746	
$Cu_{1.97}S$	hexagonal	-9.903	0.378		-0.744	
$Cu_{1.94}S$	hexagonal	-10.402	0.380		-0.737	
$Cu_{1.94}Ag_{0.03}S$	hexagonal	-9.848	0.379	0.209	-0.740	

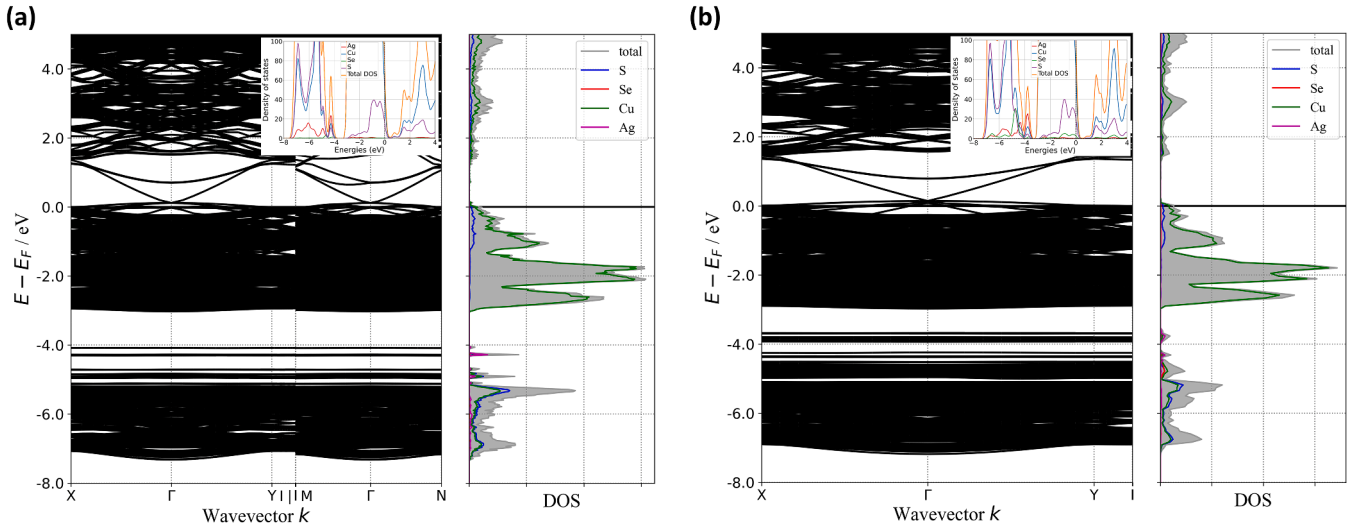

Fig. 4. Electronic band structure of $Cu_{1.94}Ag_{0.03}VA_{0.03}S_{0.99}Se_{0.01}$ (a) and $Cu_{1.94}Ag_{0.03}VA_{0.03}S_{0.10}Se_{0.10}$ (b) along with the corresponding projected density of states (DOS) in cubic symmetry. Results obtained using mBJ functional. The Fermi level is set as the energy reference.

This is evidenced in Table 1, which shows that the presence of Se leads to a reduction in electron charge, indicating a stronger covalent bonding state. Another consequence of Se doping is the associated slightly lower formation energy compared to pure S-based compounds, indicating enhanced thermodynamic stability.

3.3. Electrical transport property

The electrical transport properties of $Cu_{1.93}Ag_xS_{1-y}Se_y$ were systematically investigated in the 300 K - 873 K range. Take into account the metastability of the as-synthesized samples (as discussed in the structural section), the transport properties were thoroughly examined over multiple testing rounds. Our findings revealed that the properties became stable and reproducible starting from the second round for the representive $Cu_{1.93}Ag_{0.04}S_{0.90}Se_{0.10}$ (Fig. S10), thus, all reported measurements correspond to the second round of testing.

Starting from the room temperature properties, all the samples showed a positive Seebeck coefficient, indicating the *p*-type semiconductor character independent of the chemical composition (Fig. 5a and Fig. S11a,d). The temperature dependent trend of α and σ were strongly correlated with the phase transition beside the $Cu_{1.93}S$, and three stages could be separated: Monoclinic phase stage (M), Hexagonal phase stage (H) and Cubic phase stage (C). Firstly, the σ of the pristine $Cu_{1.93}S$ sample increases with temperature up to 573 K, which corresponds to the monoclinic (M), hexagonal (H), and the early stage of the cubic (C) phase. This increase can be attributed to thermally excited carriers that enhance the carrier concentration, thereby improving σ, where we can also find similar trend from literature [48]. Although a phase transition occurs within this temperature range, the overall increasing trend of σ remains, as the impact of lattice vibrations on carrier mobility is relatively weak. Beyond 573 K, the σ of the pristine $Cu_{1.93}S$ sample exhibits a gradual decline with increasing temperature, which is likely indicative of a transition from semiconducting to metallic characteristics [49]. However, for the samples with Ag/Ag-Se doping, the Seebeck coefficient (α) increased initially at the M stage then decreased at the H stage with the temperature increasing before re-increased at the end of H stage and in the C stage. It aligns with the structural transition observed through HT-XRD and further attests to the intricate changes in electronic transport. In fact, α and σ gradually increase as the temperature rising during the M phase stage agreed with a semiconductor (S-C) behavior and increasing of thermally excited holes. But with the shift toward the hexagonal phase, a transitional behavior is observed between 373 K - 473 K. The band gap became broader independently to the chemical composition [49] and the change in the DOS near Fermi level is highly sensitive to the Cu vacancies (Fig. 3a–d) which likely induced ambiguous behavior at the edge of the intrinsic and degenerate S-C behavior. It experimentally results in a slight decrease of α up to 473 K before it increases again while the σ constantly increase with T. With the main phase transferred from the hexagonal phase to cubic phase, the α gradually increased which could be attributed to the increased symmetry from the hexagonal phase to cubic phase inducing the degeneracy of the band gap (Fig. 3) benefiting largely to the overall electronic transport [48]. The temperature dependance of $Cu_{1.93}Ag_xS_{1-y}Se_y$ (x = 0.02, 0.04, 0.04) (y = 0, 0, 0.1) series electrical properties showed similar trend than the pristine sample with a clear dependence to the two phase transition shifted accordingly with the higher transition temperature observed through the structural analysis (Fig. 1d–f) [50]. The σ decreased with the increasing of Ag/Ag-Se codoping in the whole temperature range and the α increased (Fig. 5a and Fig. S11a,d) which seem consistent with a carrier concentration reduction induced by the Ag occupying into the Cu vacancy and/or Se substituting the S site: $\alpha \propto k_B \cdot \ln(1/n)/q$, k_B is Boltzmann constant and the α is inversely proportional to the carrier concentration determined at room temperature. To understand the transport property in-depth, hall concentration (n_H) of the typical four samples were characterized. The pristine $Cu_{1.93}S$ exhibits an intrinsic high carrier concentration of $n_H = 1.94 \times 10^{21}$ cm^{-3}, as a consequence to the large amount of copper vacancies serving as holes donor effect in the lattice. The Ag insertion acts as an electron donor which gradually reduces the carrier concentration together with the increasing of Ag content (Fig. 5c). Considering that the electronic

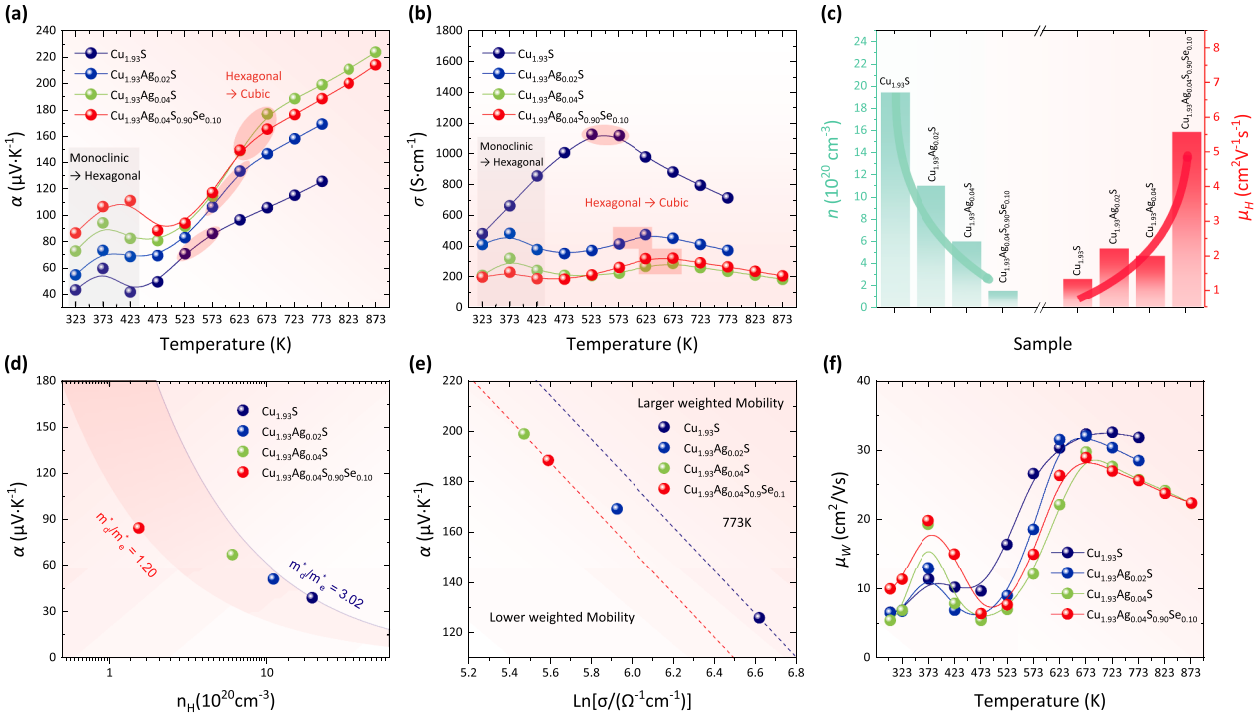

Fig. 5. Temperature dependence of (a) Seebeck coefficient (α) and (b) electrical conductivity (σ), Hall concentration and mobility at 300 K (c), (d) α versus Hall carrier concentration (n_H) (Pisarenko plot) at 300 K and (e) versus logarithm of σ (Jonker plot) at 773 K, (f) Temperature dependence of weighted mobility of bulk samples sintered at different temperatures of $Cu_{1.93}Ag_xS_{1-y}Se_y$ (x = 0, 0.02, 0.04, 0.04) (y = 0, 0, 0, 0.1).

structure does not significantly change with the Ag insertion in the high temperature structural form (Fig. 3c,d,g and h), the carrier concentration decreasing appeared in better agreement with the vacancies filling and the consequence of the Cu^{2+} content reduction into Cu^{+}. The initial charge balance of $Cu_{1.93}S$ and the Ag addition effect can be described in the following equations:

$$Cu1.93S(s) = 1.86Cu^{+} + 0.07Cu^{+} + S^{2-} \quad (1)$$

$$Cu1.93S(s) + xAg(s) = (1.86+x)Cu^{+} + (0.07-x)Cu^{2+} + xAg^{+} + S^{2-} \quad (2)$$

Subsequently, further substitution of S with Se (from $Cu_{1.93}Ag_{0.04}S$ to $Cu_{1.93}Ag_{0.04}S_{0.9}Se_{0.1}$) at room temperature will led to a partial suppression of Cu^{+} vacancy formation. This attribute to lattice expansion and the formation of stronger Cu–Se and Ag–Se bonds introduced by Se substitution, which increase the defect formation energy and will contribute to the reduction of the carrier's concentration. It is reasonable to assume that the carrier concentration reduction observed at room temperature can be transposed in the H and C stage as the α increasing gradually in the all-temperature range with the addition of Ag and Ag/Se and mostly agrees with the SPB behavior (Fig. 5d). Indeed, it highlighted a slight reduction of the effective mass m_e* with the doping and confirmed that the electronic properties are mostly driven by the carrier modulation in the M stage. Besides, the Jonker plot in the C stage (Fig. 5e) revealed a shift of the Ag/Ag-Se codoped samples following a slope of $\alpha = f(\ln(\sigma)) \propto$ -86.294 μV/K. It attests that the chemical potential variation (carrier tunning) is the origin of the electronic properties tunning and, due to the fact that weighted mobility behavior is unchanged in the whole temperature range (Fig. 5f), can be extended to the H stage [51]. The carrier tuning induced by the Ag doping act negatively on the resulting *PF* (Fig. S11c) for the high concentration of Ag, as the deflection of the σ became predominant, and justify that the Ag/Se codoping have been realized for Ag content $x = 0.04$ with the best trade-off. The Se substitution enhance drastically the μ_H (Fig. 5c) as a consequence of its respective reduced effective mass (m_d*) of $Cu_{1.93}Ag_{0.04}S_{0.9}Se_{0.1}$ (1.20 m_e*) and the increasing of the metallic character (Fig. 4). It consequently prevents the *PF* loss by cushioning the σ decreased despite the carrier concentration tunning.

3.4. Thermal transport property

The total thermal conductivity (κ) of each sample exhibits a distinct phase dependence in temperature during the two-phase transition periods, mirroring the behavior observed in the electrical transport properties (Fig. 6). The κ drastically reduced with the Ag/Ag-Se codoping and reached minimal values for the Ag-Se samples (Fig. 6a and Fig. S12). In a general description, the κ is composed of carrier contribution (κ_E) and lattice contribution (κ_L) [52]. The κ_E (Fig. 6b) can be described by Wiedemann-Franz law: $\kappa_E = L\sigma T$, where L is the Lorenz number that is obtained through the single parabolic band (SPB) model considering the acoustic phonon scattering but cannot be apply in the $Cu_{2-x}S$ system due to the superionic contribution [28]. Therefore, we define the ratio of κ_E/κ which could indirectly enable the possibility to estimate the κ_L trend (Fig. 6c) by illustrated the κ_E proportion trend. For the pristine $Cu_{1.93}S$, κ_E/κ gradually increased with the increasing temperature up to 573 K and achieved a high ratio around 90 % from 573 K to 873 K, highlighting that carrier plays the major role on thermal transport. With the Ag doping into the $Cu_{1.93}S$, the ratio of κ_E/κ decreased especially in the high temperature range. It is visible that the depletion of κ due to the Ag doping ($\Delta\kappa_{(pristine/Ag)} \approx 0.68$@773 K) cannot be entirely attributed to the decrease in κ_E ($\Delta\kappa_{E(pristine/Ag)} \approx 0.62$@773 K), which suggests a variation in κ_L through the structural influence of Ag insertion. Indeed, the Cu vacancy filling by Ag will introduce additional phonon scattering center. To probe this influence on the phonon dispersion structure, the lattice thermal properties have been analyzed through additional phonon calculations. Only cubic-based compounds, with and without Ag doping, were considered to understand its influence, as the hexagonal symmetry was too complex to be considered. The dispersion curves are presented in Fig. S13. Despite using a reasonably relaxed structure as an initial stage, few imaginary branches appeared, indicating mechanical

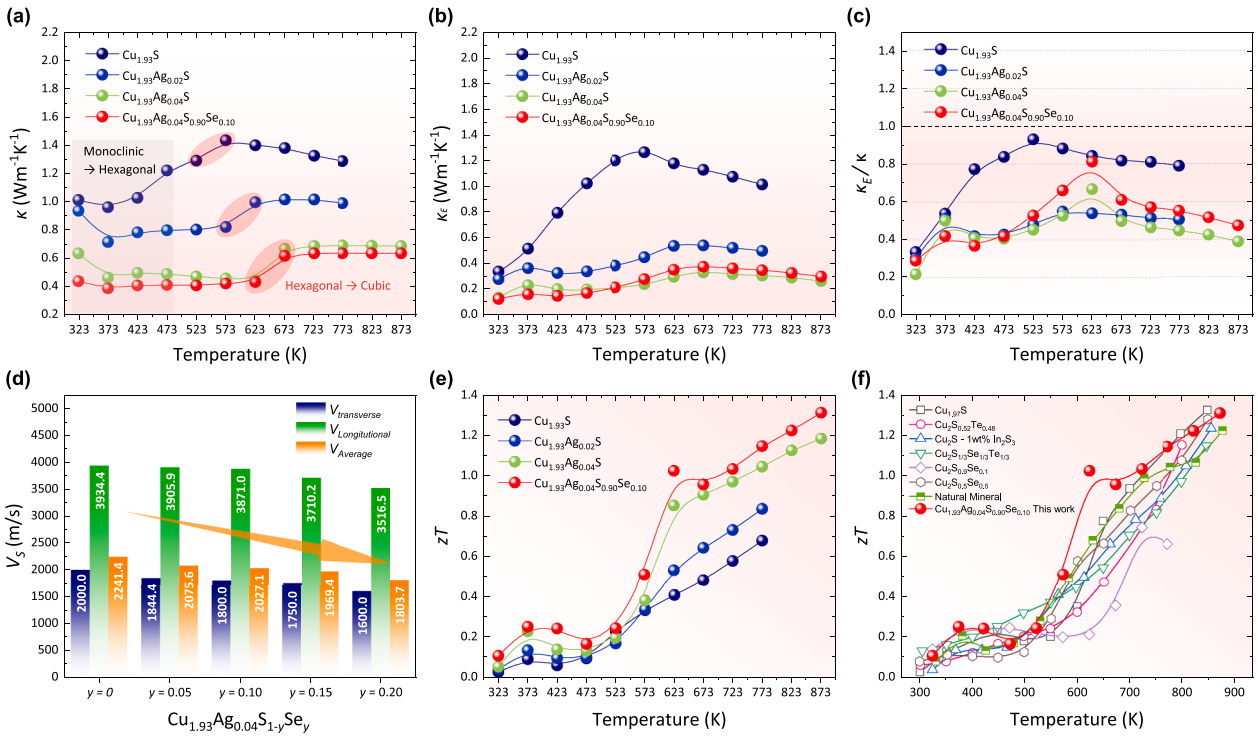

Fig. 6. Temperature dependence of thermal conductivity κ (a), Electrical thermal conductivity κ_E (b), ratio of κ_E /κ_L (c), room temperature sound of velocity for $Cu_{1.93}Ag_{0.04}S_{1-y}Se_y$ ($y = 0$, 0.05, 0.1, 0.15, 0.20) (d). Figure of merit ZT (e) for $Cu_{1.93}Ag_xS_{1-y}Se_y$ ($x = 0$, 0.02, 0.04, 0.04) ($y = 0$, 0, 0, 0.1), State of art figure of merit in Cu-S system (f).

instability at 0 K. This is not surprising since the cubic phase is not stable at low temperatures. However, as a relative comparison and with a simple approximation that neglects this metastability, it is interesting to observe a slight shift of all frequencies toward lower values upon the addition of a heavier element like Ag, even at a very small composition of x' = 0.03 which can explain the lower thermal conductivity. Furthermore, the expansion of the unit cell induced by Ag doping leads to an increased Cu-S interatomic distance, which may contribute to the development of a softer bonding effect. Consequently, the computed heat capacity C_v within the harmonic approximation (at volume constant) shows an increase for the silver-doped compounds, as depicted in Fig. S14. For a more accurate analysis, C_p should be computed using the quasi-harmonic approximation and additional corrections, though this would require significantly more computationally demanding calculations. As seen from Fig. 6a, κ furthermore reduced with the $Cu_{1.93}Ag_{0.04}S_{0.9}Se_{0.1}$ sample due to the slight additional reduction of κ most likely issue from the mass fluctuation effect which further minimize the κ_L. Experimentally, the sound velocities of all the Ag-Se codoped specimens were characterized and are exhibited in Fig. 6d. It shows that the longitudinal sound velocity ($V_{Longitudinal}$), the transverse sound velocity ($V_{Transverse}$) and the average sound velocity ($V_{Average}$) gradually decreased with Se doping which could rationalize the reduction of κ_L, according to the following equation: $\kappa_L = \frac{1}{3}C_v v_s l$ where C_v is specific heat capacity of phonons, V_s is average sound velocity, l is phonon mean free path. As the Cu-Se bond (240–270 kJ/mol) has a lower bonding strength than the Cu-S bond (285–320 kJ/mol), the low frequency local phonon mode is easier to form in the material, which could reduce the sound speed and enhances phonon scattering, resulting in lower lattice thermal conductivity. In summary, with the greatly decreased κ_E from pristine $Cu_{1.93}S$ to $Cu_{1.93}Ag_{0.04}S$ and the decreased κ_L from $Cu_{1.93}Ag_{0.04}S$ to $Cu_{1.93}Ag_{0.04}S_{0.9}Se_{0.1}$, we get low thermal conductivity in the high temperature region.

Following the carrier concentration tuning and the increasing of lattice scattering, a competitive figure of merit zT is obtained with the $Cu_{1.93}$ $Ag_{0.04}S_{0.9}Se_{0.1}$ sample (Fig. 6e) with a top value reaching zT = 1.33 at the modest temperature of 873 K, which correspond to one of the highest zT among current state of art Cu – S binary system (Fig. 6f).

3.5. Electrical and thermal stability

In this study, the stability under electrical current stress and the high temperature of our samples were investigated. We selected the pristine $Cu_{1.93}S$ sample, $Cu_{1.93}Ag_{0.04}S_{0.9}Se_{0.1}$ sample and the $Cu_{1.97}S$ as a reference for comparison with the Ag-Se codoping sample with the same vacancy filling level. The length of all samples was 8 mm, and the current density set as 12 A/cm^2. As shown from Fig. 7a, the representative ratio of the electrical degradation (R/R_0) of $Cu_{1.93}S$ sample sharply decreased to 90 % of initial resistivity after 3 h before stabilized to similar values after 24 h. The R/R_0 of $Cu_{1.97}S$ sample also sharply decreased to 80 % of initial resistivity after 2 h aging. It confirmed the relatively poor electrical stability of the binary composition, especially in the case of a reduced Cu vacancy concentration ($Cu_{1.97}S$). Comparably, the R/R_0 of $Cu_{1.93}Ag_{0.04}S_{0.9}Se_{0.1}$ keeps a relatively high ratio, which means that after filling Ag into Cu vacancies and Se substituting into S site, the Cu ion migration is efficiently suppressed. This result evidenced the underlining steric confinement mechanism which could be described below: although Ag^+ is also a mobile ion like Cu^+, the Ag^+ with larger ionic radius and distinct electronic configuration could partially occupy the Cu^+ site to reduce the vacancy formation which will lead to local lattice expansion, thereby altering the potential energy landscape for Cu^+ migration. This modification increases the migration energy barrier and effectively suppresses Cu^+ hopping [36,47]. Besides, our calculation in the high-temperature cubic phase (Fig. 4) revealed the formation of low-energy 4d bands around -4 eV by the Ag, below the 3d states of copper, which may play a role in limiting metal diffusion by adding a contribution to the energy barrier. Finally, the ionic confinement is also enhanced by the geometric criteria, as the interaction distance increases with the doping element, which limits the diffusion of metallic atom by steric effect (Fig. 2 and Fig. S9). With the increased energy barrier created by steric confinement, the copper migration is consequently suppressed.

In parallel, we performed the thermal stability testing with the pristine $Cu_{1.93}S$, $Cu_{1.93}Ag_{0.02}S$, $Cu_{1.93}Ag_{0.04}S$ and $Cu_{1.93}Ag_{0.04}S_{0.9}Se_{0.1}$ (Fig. 7b). The temperature procedure has been designed to keep the respective temperature (673 K, 773 K, 873 K, 973 K) for 1 h. It can be clearly observed a mass loss for the pristine $Cu_{1.93}S$ sample after heating up to 973 K under Ar atmosphere. With the Ag doping and Ag-Se codoping, the mass loss is nullified attesting to superior thermal stability for temperature above 873 K in comparison with the pristine sample. Such chemical enhanced thermal stability is most likely originated from the improved structural stability induced by the Ag doping confirmed above (cf. Structural part). It has been observed that doping compounds eliminate metastability and increase the temperature at which the material transitions to a cubic phase (Fig. 1 and Fig. S7) and was supported by DFT calculations (Fig. S8). Indeed, the difference in the enthalpy of formation between the hexagonal and cubic phases is larger for $Cu_{1.94}Ag_{0.03}S$ (4.057 kJ/mol) compared to the undoped compound (3.279 kJ/mol) evidencing that the hexagonal structure remains stable over a wider temperature range, which is consistent with enhanced thermal stability in the cubic phase. As a result, it demonstrates that Ag and Ag-Se codoping strategy would also create thermally stable sample with optimal composition of $Cu_{1.93}Ag_{0.04}S_{0.9}Se_{0.1}$.

4. Conclusion

In this study, a series of quaternary $Cu_{1.93}Ag_xS_{1-y}Se_y$ (x = 0, 0.02,

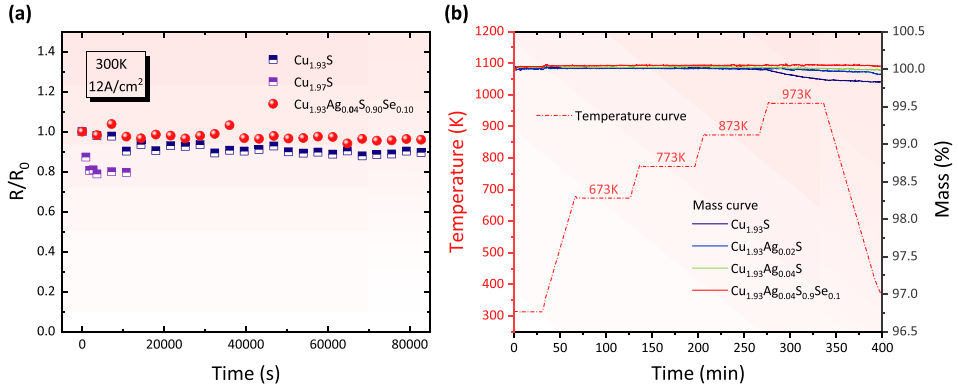

Fig. 7. Room temperature current stability testing (R/R_0) of $Cu_{1.93}S$, $Cu_{1.97}S$, $Cu_{1.93}Ag_{0.04}S_{0.9}Se_{0.1}$ under the current density of 12 A/cm^2 (a), thermal stability testing of $Cu_{1.93}S$, $Cu_{1.93}Ag_{0.02}S$, $Cu_{1.93}Ag_{0.04}S$, $Cu_{1.93}Ag_{0.04}S_{0.9}Se_{0.1}$ (b).

0.04, 0.07) (y = 0, 0.05, 0.10, 0.15, 0.20) chalcogenides were synthesized and their influence on the structural, physicochemical, and thermoelectric properties of the corresponding bulk samples systematically investigated. Room temperature XRD shows that the pristine $Cu_{1.93}S$ exhibits a metastable tetragonal phase where it could transfer into a monoclinic phase after exposing into the vacuum condition for 60 days. However, we have evidence that the Ag and Ag-Se codoping promotes superior structural stability. The in-depth analysis of the High Temperature X-ray diffraction (HT-XRD) and elemental analysis sustain that the Ag and Se substitute the Cu vacancies and S site respectively. Moreover, thanks to the HT-XRD combined with the calorimetry analysis (DSC signal), we showed that the different temperature of phase transition from hexagonal phase to cubic phase shifted toward higher temperature in respect with the presence of Ag and Ag-Se element within the structure. From a transport point of view, the investigation of electrical transport properties revealed that Ag doping acts as an electron donor, leading to a reduction in carrier concentration. Meanwhile, Se co-doping decreases the effective mass of charge carriers and promote a superior carrier mobility limiting the *PF* loss in the codoped composition. Regarding thermal transport, Ag doping contributes to an overall reduction in total thermal conductivity, while Se co-doping further lowers lattice thermal conductivity, reinforcing the decrease in total thermal conductivity. Furthermore, thanks to the Ag filling into Cu vacancies and Se substituting into S site, the Cu ion migration suppressed compared to the Cu_xS (with $1.93 < x < 1.97$), the thermal stability of $Cu_{1.93}Ag_{0.04}S_{0.9}Se_{0.1}$ was also improved compared to the $Cu_{1.93}S$. The theoretical analysis, through DFT calculation on complex modelized $Cu_xAg_{x'}Va_{2-x-x'}S_{1-y}Se_y$ compounds, corroborated the experimental findings, demonstrating that Se substitution and Ag doping effectively modulate the electronic band structure and phonon dispersion, respectively, contributing to the observed enhancement of thermoelectric performance and stability by manipulating the energy barrier. Combining the Ag and Se doping, we finally obtain a competitive figure of merit zT (1.33@873 K) with the $Cu_{1.93}Ag_{0.04}S_{0.9}Se_{0.1}$ sample demonstrating the attractiveness of synergically combine those two elements as dopant in $Cu_{2-x}S$ system in order to design electrically and thermally stable *p*-type thermoelectric material in the intermediate temperature.

CRediT authorship contribution statement

Xinyuan Wang: Writing – original draft, Investigation. **Cédric Bourgès:** Writing – review & editing, Supervision, Methodology, Conceptualization. **Jean-Claude Crivello:** Writing – review & editing, Investigation, Formal analysis. **Takao Mori:** Writing – review & editing, Supervision, Project administration, Funding acquisition, Conceptualization.

Declaration of competing interest

The authors declare that they have no known competing financial interests or personal relationships that could have appeared to influence the work reported in this paper.

Acknowledgments

This work was supported by JST Mirai Program JPMJMI19A1 and International Center for Young Scientist (ICYS) Fellowship. Xinyuan Wang gratefully acknowledges financial support from the China Scholarship Council (CSC). The authors would like to acknowledge Material Analysis Station (NIMS, Japan) for the XRD analysis. This work was supported by "Advanced Research Infrastructure for Materials and Nanotechnology in Japan (ARIM)" of the Ministry of Education, Culture, Sports, Science and Technology (MEXT). Proposal Number JPMXP1223NM5150. DFT calculations were performed using French HPC resources of GENCI–TGCC (Grant A0060906175).

Supplementary materials

Supplementary material associated with this article can be found, in the online version, at doi:10.1016/j.actamat.2025.121424.

References

[1] E.S.T.G.Jeffrey Snyder, Complex thermoelectric materials, Nat. Mater. 7 (2008) 105–114, https://doi.org/10.1038/nmat2090.
[2] L.E. Bell, Cooling, heating, generating power, and recovering waste heat with thermoelectric systems, Science 321 (2008) 1457–1461, https://doi.org/10.1126/science.1158899.
[3] T. Mori, Novel principles and nanostructuring methods for enhanced thermoelectrics, Small 13 (2017) 1702013, https://doi.org/10.1002/smll.201702013.
[4] T. Hendricks, T. Caillat, T. Mori, Keynote review of latest advances in thermoelectric generation materials, devices, and technologies, Energies (Base I) 15 (2022) 7307, https://doi.org/10.3390/en15197307.
[5] L. Hu, H. Wu, T. Zhu, C. Fu, J. He, P. Ying, X. Zhao, Tuning multiscale microstructures to enhance thermoelectric performance of *n*-type bismuth-telluride-based solid solutions, Adv. Energy Mater. 5 (2015) 1500411, https://doi.org/10.1002/aenm.201500411.
[6] B. Zhu, X. Liu, Q. Wang, Y. Qiu, Z. Shu, Z. Guo, Y. Tong, J. Cui, M. Gu, J. He, Realizing record high performance in *n*-type Bi_2Te_3-based thermoelectric materials, Energy Environ. Sci. 13 (2020) 2106–2114, https://doi.org/10.1039/D0EE01349H.
[7] M. Hirschberger, J.W. Krizan, R.J. Cava, N.P. Ong, Dense dislocation arrays embedded in grain boundaries for high-performance bulk thermoelectrics, Science 348 (2015) 106–109, https://doi.org/10.1126/science.aaa4166.
[8] Y. Pei, X. Shi, A. Lalonde, H. Wang, L. Chen, G.J. Snyder, Convergence of electronic bands for high performance bulk thermoelectrics, Nature 473 (2011) 66–69, https://doi.org/10.1038/nature09996.
[9] C. Liu, Z. Zhang, Y. Peng, F. Li, L. Miao, E. Nishibori, R. Chetty, X. Bai, R. Si, J. Gao, X. Wang, Y. Zhu, N. Wang, H. Wei, T. Mori, Charge transfer engineering to achieve extraordinary power generation in GeTe-based thermoelectric materials, Sci. Adv. 9 (2023) eadh0713, https://doi.org/10.1126/sciadv.adh0713.
[10] L.D. Zhao, S.H. Lo, Y. Zhang, H. Sun, G. Tan, C. Uher, C. Wolverton, V.P. Dravid, M. G. Kanatzidis, Ultralow thermal conductivity and high thermoelectric figure of merit in SnSe crystals, Nature 508 (2014) 373–377, https://doi.org/10.1038/nature13184.
[11] J. Mao, H. Zhu, Z. Ding, Z. Liu, G.A. Gamage, G. Chen, Z. Ren, High thermoelectric cooling performance of *n*-type Mg_3Bi_2-based materials, Science 365 (2019) 6452, https://doi.org/10.1126/science.aax7792.
[12] Z. Liu, W. Gao, H. Oshima, K. Nagase, C.H. Lee, T. Mori, Maximizing the performance of *n*-type Mg_3Bi_2 based materials for room-temperature power generation and thermoelectric cooling, Nat. Commun. 13 (2022) 1120. https://www.nature.com/articles/s41467-022-28798-4.
[13] A.V. Powell, Recent developments in Earth-abundant copper-sulfide thermoelectric materials, J. Appl. Phys. 126 (2019) 10090, https://doi.org/10.1063/1.5115708.
[14] P. Kamińska, C. Bourgès, R. Chetty, D. Gutiérrez-Del-Río, P. Śpiewak, W. Święszkowski, T. Nishimura, T. Mori, Insight into the preponderant role of the lattice size in Sn-based colusites for promoting a high power factor, J. Mater. Chem. A. 10 (2022) 10701–10704, https://doi.org/10.1039/d2ta01210c.
[15] C. Bourgès, G. Lambard, N. Sato, M. Tachibana, S. Ishii, T. Mori, Process optimization on kesterite-based ceramics for enhancing their thermoelectric performances assisted by active machine learning approach: A tool for metal-sulfide ceramics development, Acta. Mater. 281 (2024) 120342, https://doi.org/10.1016/j.actamat.2024.120342.
[16] G. Guélou, P. Lemoine, B. Raveau, E. Guilmeau, Recent developments in high-performance thermoelectric sulphides: an overview of the promising synthetic colusites, J. Mater. Chem. C 9 (2021) 773–795, https://doi.org/10.1039/d0tc05086e.
[17] O. Caballero-Calero, J.R. Ares, M. Martín-González, Environmentally Friendly Thermoelectric Materials: High Performance from Inorganic Components with Low Toxicity and Abundance in the Earth, Adv. Sustain. Syst. 5 (2021) 2100095, https://doi.org/10.1002/adsu.202100095.
[18] N. Tsujii, T. Mori, High thermoelectric power factor in a carrier-doped magnetic semiconductor $CuFeS_2$, Appl. Phys. Express. 6 (2013) 043001, https://doi.org/10.7567/APEX.6.043001.
[19] R. Ang, A.U. Khan, N. Tsujii, K. Takai, R. Nakamura, T. Mori, Thermoelectricity Generation and Electron–Magnon Scattering in a Natural Chalcopyrite Mineral from a Deep-Sea Hydrothermal Vent, Angew. Chem. 127 (2015) 13101–13105, https://doi.org/10.1002/ange.201505517.
[20] F.H. Sun, H. Li, J. Tan, L. Zhao, X. Wang, H. Hu, C. Wang, T. Mori, Review of current $ZT > 1$ thermoelectric sulfides, J. Materiomics 10 (2024) 218–233, https://doi.org/10.1016/j.jmat.2023.05.011.
[21] Y. He, T. Day, T. Zhang, H. Liu, X. Shi, L. Chen, G.J. Snyder, High thermoelectric performance in non-toxic earth-abundant copper sulfide, Adv. Mater. 26 (2014) 3974–3978, https://doi.org/10.1002/adma.201400515.
[22] T.Y. Yang, Z.Y. Wang, X. Yan, C.Y. Wang, Y.X. Zhang, Z.H. Ge, J. Feng, Excellent thermoelectric performance realized in copper sulfide magnetic nanocomposites via modified solid states reaction, Adv. Sci. 12 (2025) 2198–3844, https://doi.org/10.1002/advs.202409494.

[23] S. Song, T. Saito, S. Lee, M. Hagihala, Y. Ishikawa, S. Torii, K. Mori, S. Itoh, K. S. Lee, D.Y. Cho, T. Kamiyama, Evidence of tuned anharmonicity in the thermoelectric material $Cu_{2-x}S$, Commun. Mater. 6 (2025) 60, https://doi.org/10.1038/s43246-025-00775-6.
[24] G. Dennler, R. Chmielowski, S. Jacob, F. Capet, P. Roussel, S. Zastrow, K. Nielsch, I. Opahle, G.K.H. Madsen, Are binary copper sulfides/selenides really new and promising thermoelectric materials? Adv. Energy Mater. 4 (2014) 1301581 https://doi.org/10.1002/aenm.201301581.
[25] P. Qiu, M.T. Agne, Y. Liu, Y. Zhu, H. Chen, T. Mao, J. Yang, W. Zhang, S.M. Haile, W.G. Zeier, J. Janek, C. Uher, X. Shi, L. Chen, G.J. Snyder, Suppression of atom motion and metal deposition in mixed ionic electronic conductors, Nat. Commun. 9 (2018) 2910, https://doi.org/10.1038/s41467-018-05248-8.
[26] Z.H. Ge, B.P. Zhang, Y.X. Chen, Z.X. Yu, Y. Liu, J.F. Li, Synthesis and transport property of $Cu_{1.8}S$ as a promising thermoelectric compound, Chem. Commun. 47 (2011) 12697–12699, https://doi.org/10.1039/c1cc16368j.
[27] Z. Zhao, D.D. Liang, J. Pei, J.L. Shi, Y. Wu, R. Zhang, B.P. Zhang, Enhanced thermoelectric properties of $Mn_xCu_{1.8}S$ via tuning band structure and scattering multiscale phonons, J. Materiomics 7 (2021) 556–562., https://doi.org/10.1016/j.jmat.2020.11.001.
[28] Y. Zhang, C. Xing, Y. Liu, M.C. Spadaro, X. Wang, M. Li, K. Xiao, T. Zhang, P. Guardia, K.H. Lim, A.O. Moghaddam, J. Llorca, J. Arbiol, M. Ibáñez, A. Cabot, Doping-mediated stabilization of copper vacancies to promote thermoelectric properties of $Cu_{2-x}S$, Nano Energy 85 (2021) 105991, https://doi.org/10.1016/j.nanoen.2021.105991.
[29] Y.X. Zhang, Q. Lou, Z.H. Ge, S.W. Gu, J.X. Yang, J. Guo, Y.K. Zhu, Y. Zhou, X.H. Yu, J. Feng, J. He, Excellent thermoelectric properties and stability realized in copper sulfides based composites via complex nanostructuring, Acta Mater. 233 (2022) 105991, https://doi.org/10.1016/j.actamat.2022.117972.
[30] Y.X. Zhang, T.Y. Yang, Z.Y. Wang, J. Feng, Z.H. Ge, Highly enhanced stability and thermoelectric performance of copper sulfides-based composites by multiphase engineering, Mater. Today Phys. 27 (2022) 100808, https://doi.org/10.1016/j.mtphys.2022.100808.
[31] H. Tang, F.H. Sun, J.F. Dong, H.L.Zhuang Asfandiyar, Y. Pan, J.F. Li, Graphene network in copper sulfide leading to enhanced thermoelectric properties and thermal stability, Nano Energy 49 (2018) 267–273., https://doi.org/10.1016/j.nanoen.2018.04.058.
[32] T. Mao, P. Qiu, J. Liu, X. Du, P. Hu, K. Zhao, D. Ren, X. Shi, L. Chen, Good stability and high thermoelectric performance of Fe doped $Cu_{1.80}S$, Phys. Chem. Chem. Phys. 22 (2020) 7374–7380., https://doi.org/10.1039/d0cp00733a.
[33] X. Wang, C. Bourgès, N. Sato, C.L. Hassam, T. Mori, Process influence on thermoelectric performance of digenite ($Cu_{1.8}S$) and its underlined thermal instability, Ceram. Int. 51 (2025) 10443–10452, https://doi.org/10.1016/j.ceramint.2024.12.477.
[34] Q.L. Meng, S. Kong, Z. Huang, Y. Zhu, H.C. Liu, X. Lu, P. Jiang, X. Bao, Simultaneous enhancement in the power factor and thermoelectric performance of copper sulfide by In_2S_3 doping, J. Mater. Chem. A. 4 (2016) 12624–12629, https://doi.org/10.1039/c6ta03780a.
[35] Z.H. Ge, Y.X. Zhang, T.Y. Yang, D. He, Y. Xiao, H. Lai, Y. Wang, J. Deng, J.F. Li, J. Feng, J. He, L.D. Zhao, Highly stabilized thermoelectric performance in natural minerals, Joule 8 (2024) 129–140, https://doi.org/10.1016/j.joule.2023.11.013.
[36] H. Hu, Y. Ju, J. Yu, Z. Wang, J. Pei, H.C. Thong, J.W. Li, B. Cai, F. Liu, Z. Han, B. Su, H.L. Zhuang, Y. Jiang, H. Li, Q. Li, H. Zhao, B.P. Zhang, J. Zhu, J.F. Li, Highly stabilized and efficient thermoelectric copper selenide, Nat. Mater. 23 (2024) 527–534, https://doi.org/10.1038/s41563-024-01815-1.
[37] Y. Yao, B.P. Zhang, J. Pei, Y.C. Liu, J.F. Li, Thermoelectric performance enhancement of Cu_2S by Se doping leading to a simultaneous power factor increase and thermal conductivity reduction, J. Mater. Chem. C. 5 (2017) 7845–7852, https://doi.org/10.1039/c7tc01937h.
[38] A. Zunger, S.H. Wei, L.G. Ferreira, J.E. Bernard, Special quasirandom structures, Phys. Rev. Lett. 65 (1990) 353–356, https://doi.org/10.1103/PhysRevLett.65.353.
[39] A. van de Walle, M. Asta, G. Ceder, The alloy theoretic automated toolkit: a user guide, Calphad. 26 (2002) 539–553, https://doi.org/10.1016/S0364-5916(02)80006-2.
[40] A. van de Walle, P. Tiwary, M. de Jong, D.L. Olmsted, M. Asta, A. Dick, D. Shin, Y. Wang, L.-Q. Chen, Z.-K. Liu, Efficient stochastic generation of special quasirandom structures, Calphad. 42 (2013) 13–18, https://doi.org/10.1016/j.calphad.2013.06.006.
[41] G. Kresse, J. Furthmüller, Efficiency of ab-initio total energy calculations for metals and semiconductors using a plane-wave basis set, Comput. Mater. Sci. 6 (1996) 15–50, https://doi.org/10.1016/0927-0256(96)00008-0.
[42] J.P. Perdew, K. Burke, M. Ernzerhof, Generalized gradient approximation made simple, Phys. Rev. Lett. 77 (1996) 3865–3868, https://doi.org/10.1103/PhysRevLett.77.3865.
[43] A.D. Becke, E.R. Johnson, A simple effective potential for exchange, J. Chem. Phys. 124 (2006) 221101, https://doi.org/10.1063/1.2213970.
[44] H.T. Evans, The crystal structures of low chalcocite and djurleite Zeitschrift für Kristallographie, J. us Geological Survey 150 (1979) 299–320, https://doi.org/10.1524/zkri.1979.150.14.299.
[45] T. Ohtani, M. Motoki, K. Koh, K. Ohshima, Synthesis of binary copper chalcogenides by mechanical alloying, Mater. Res. Bull. 30 (1995) 1495–1504., https://doi.org/10.1016/0025-5408(95)00155-7.
[46] M.Y. Posrr, P.R. Busncr, Djurleite, digenite, and chalcocite: Intergrowths and transformations, Am. Mineral. 79 (1994) 34. https://pubs.geoscienceworld.org/msa/ammin/article-abstract/79/3-4/308/42881/.
[47] A. Mikuła, Structural and electronic properties of Ag-, Ni-, and Zn-doped copper chalcogenides – computational studies, Mater. Today Commun. 40 (2024) 109913, https://doi.org/10.1016/j.mtcomm.2024.109913.
[48] Q. Xu, B. Huang, Y. Zhao, Y. Yan, R. Noufi, S.H. Wei, Crystal and electronic structures of Cu_xS solar cell absorbers, Appl. Phys. Lett. 100 (2012) 6, https://doi.org/10.1063/1.3682503.
[49] Y.X. Zhang, Q.Y. Huang, X. Yan, C.Y. Wang, T.Y. Yang, Z.Y. Wang, Y.C. Shi, Q. Shan, J. Feng, Z.H. Ge, Synergistically optimized electron and phonon transport in high-performance copper sulfides thermoelectric materials via one-pot modulation, Nat. Commun. 15 (2024) 2736, https://doi.org/10.1038/s41467-024-47148-0.
[50] G.J. Snyder, A.H. Snyder, M. Wood, R. Gurunathan, B.H. Snyder, C. Niu, Weighted mobility, Adv. Mater. 32 (2020) 25, https://doi.org/10.1002/adma.202001537.
[51] A. Novitskii, T. Mori, Pisarenko's Formula for the Thermopower. http://arxiv.org/abs/2502.03837, 2025.
[52] H.S. Kim, Z.M. Gibbs, Y. Tang, H. Wang, G.J. Snyder, Characterization of Lorenz number with Seebeck coefficient measurement, Apl. Mater. 3 (2015) 041506, https://doi.org/10.1063/1.4908244.